land

MDPI

Article

Study on the Deformation of Filling Bodies in a Loess Mountainous Area Based on InSAR and Monitoring Equipment

Yuming Wu [1] and Hengxing Lan [1,2,*]

[1] State Key Laboratory of Resources and Environmental Information System, Institute of Geographic Sciences and Natural Resources Research, Chinese Academy of Sciences, Beijing 100101, China
[2] College of Geological Engineering and Geomatics, Chang'an University, Xi'an 710054, China
* Correspondence: lanhx@lreis.ac.cn

Abstract: Several land-creation projects, such as the Lanzhou New Area (LNA), have been undertaken in China as part of the Belt and Road Initiative to bring more living space to the local people in loess areas. However, undisturbed loess and remolded loess have different mechanical characteristics, which may influence the stability of the filling process. Therefore, we monitored the deformation through InSAR and field monitoring to investigate the deformation characteristics and their causes. We obtained the horizontal and vertical displacements, internal deformation, water content, and pressure, according to the air–space–ground integrated monitoring technique. The results show that stress and deformation increase rapidly during construction. Deformation in different places is different during the winter: (1) for vertical displacement, uplift is present in the cut area, settlement is present in the fill area, and heterogeneity is evident in other areas; (2) for horizontal displacement, the expansion state is present in the filling area and the compression state is present at the boundary. Laboratory tests show that the difference in soil compression properties is one of the reasons for these deformation characteristics. Additionally, the difference in volumetric water content and permeability coefficient may trigger different mechanical properties on both sides of the boundary. All the evidence indicates that the boundary region is critical for filling projects. It is also necessary to install monitoring equipment to observe deformation. When abnormal deformations appear, we should take measures to control them.

Keywords: InSAR; loess; in situ; deformation; land creation

Citation: Wu, Y.; Lan, H. Study on the Deformation of Filling Bodies in a Loess Mountainous Area Based on InSAR and Monitoring Equipment. *Land* **2022**, *11*, 1263. https://doi.org/10.3390/land11081263

Academic Editors: Stefano Morelli, Veronica Pazzi and Mirko Francioni

Received: 28 June 2022
Accepted: 5 August 2022
Published: 7 August 2022

1. Introduction

Loess, one of the quaternary sediments, is widely distributed in China, covering approximately 440,000 km^2 [1,2]. The Loess Plateau is a plateau in north-central China formed of loess. It is one of the important agricultural regions in China, covering an area of 624,641 km^2 and supporting 17% of the population [3]. Additionally, there is not enough space for downtown areas to expand in these places. Lanzhou is an important city in western China, but it is located in a valley, which seriously hinders urban development [4]. A total of 57% of the area of Lanzhou comprises unused land such as barren hills, gentle slopes, and gullies; filling gullies to create farmland on the Loess Plateau can help to solve many problems. As part of the strategy of Western Development and the Belt and Road Initiative, several loess projects have been initiated, such as the Lanzhou New Area (LNA) [5], which consists of more than 250 square kilometers of reclaimed land [6]. The maximum annual average expansion rate was about 36 km^2/a from 2012 to 2016 [7]. These projects will give people more new flat land and more ground for agriculture [8], but that comes with risks in the absence of carefully designed engineering controls [6,9].

Loess, a clastic, predominantly silt-sized sediment, has a metastable structure [10–12] and is composed of million-year-old thick deposits of windblown dust and silt. The grain sizes range from 0.005 to 0.05 mm, and the porosity generally ranges from 42% to 55% [13].

The loess structure produces collapsibility, which induces sharp sinking and causes ground deformation when it encounters water. At the micro level, debonding, grain crushing, and fabric transition appear during collapse; at the macro level, creeping and softening appear when the structure changes. According to Wen and Yan [14], the shear strength reduction in loess due to structural characteristics should be attributed to the breaking of cementation bonds between particles. The different physical and mechanical properties make construction difficult, especially for filling and excavation projects; consequently, researchers have designed several experiments to explore such geotechnical properties in order to address these problems [15–17].

Loess, a strongly collapsible soil, easily softens and deforms when it encounters water. The penetration of water into loess is very complicated: after water infiltrates the pores of the undisturbed loess, the moisture content and matric suction of the loess will change, and its shear strength will be reduced significantly [18,19]. In some studies, undisturbed loess is stronger than remolded loess at the same density and water content [20]. The experimental results show that mechanical parameters such as the shear strength, compressive strength, and Young's modulus of undisturbed loess and remolded loess are significantly different. Differential deformation with different properties is one of the factors that trigger geohazards [21–23]; therefore, this variability in soil properties can cause problems in filling projects. However, the deformation process at the boundary is unclear for loess-filling projects.

For displacement monitoring, GPS is the best real-time monitoring technique to monitor surface deformation, especially for landslide displacement [24]. For large-scale monitoring, InSAR observations are the favored tool and have been successfully applied in mountains and plains [25,26], glacier monitoring [27], urban subsidence monitoring [28], and landslide monitoring [29]. Large-scale loess deformation has also been observed using this technique [5,30–32]. From monitoring loess filling projects, it has been found that deformation generally occurs on the edge of the cutting and filling slope; in the LNA, there is significant subsidence after filling from large-scale observations. In addition, the spatial heterogeneity of land creation results in different deformation modes [5]. After land reclamation in loess areas, the stress changes, amounting to hundreds of kilopascals in shallow zones, which, in turn, induce deformations in the filling bodies [33]. Based on monitoring studies, the surface subsidence is mainly located in the filling area [34,35], while uplifting occurs in the excavation area [36].

In this paper, we monitored the surface deformation process in the study area through ascending and descending images during the winter and buried equipment such as displacement meters to monitor the internal deformation. Additionally, we buried moisture meters and earth pressure cells to investigate the reasons for such changes. Based on the space–air–ground integrated monitoring technique, we analyzed the deformation characteristics of loess during the winter.

2. Study Area

Lanzhou city, Gansu, located in northwestern China (Figure 1A), is an important regional commercial center and transportation hub. Due to the U-shaped and V-shaped valleys around the city and the Yellow River that crosses the city, the topography hampers the development of Lanzhou. Lanzhou creates more land for development by filling the loess valley and cutting the loess mountain; in the LNA in particular, hundreds of mountain tops have been flattened.

The LNA, founded in 2012, is a state-level new area that spans 40 km north to south and 16 km east to the west. It is located 30 km from Lanzhou's old city in the Qinwangchuan Plain, which is the largest plateau basin near Lanzhou (Figure 1A). Local governments removed the tops of many high loess mountains to fill the adjacent valleys to create new flat land for living space and agriculture. In this area, it has a typical semiarid continental monsoon climate. The average temperature is approximately 4.1 °C, and the typical annual precipitation is 300–500 mm, with almost 60% of the precipitation occurring in the

summer [5]. There have been many filling projects from 2002 to 2022 (Figure 1B). Our study area is located in the southeast of the LNA, which is set to provide sufficient land for local agriculture in the future.

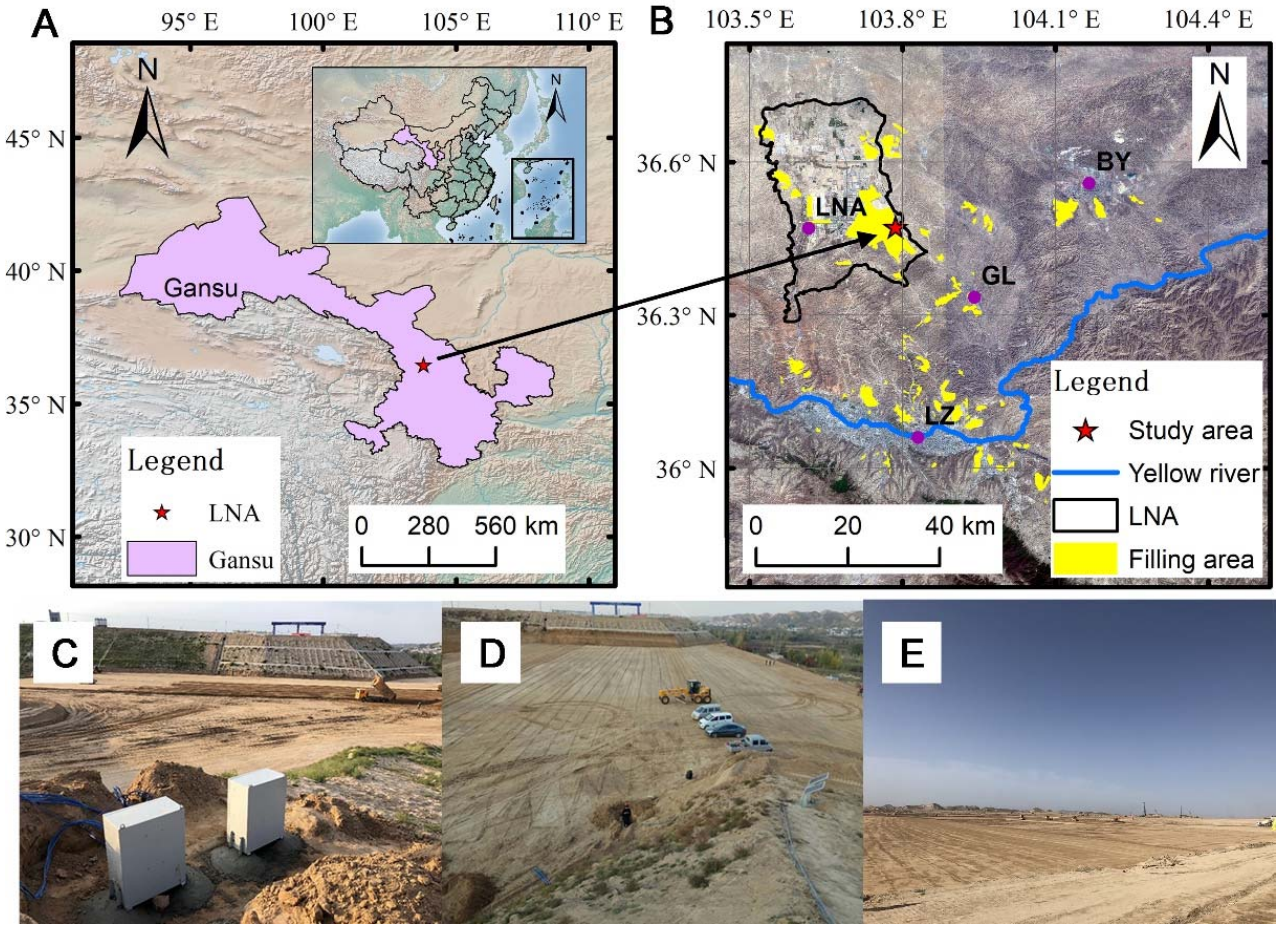

Figure 1. Study area and photos of different stages ((**A**) is the location of the research area, (**B**) is the distribution of the filling areas in Lanzhou, (**C**) is a photo of our research area taken on 12 September 2018, (**D**) is a photo of our research area taken on 16 October 2018, and (**E**) is a photo of our research area taken on 6 June 2019. LZ: Lanzhou city, GL: Gaolan county, BY: Baiyin city).

In this project, the construction process is divided into five steps: (1) cutting the slope into steps; (2) filling 30 cm at a time; (3) watering it to achieve the optimal moisture content; (4) rolling it to achieve the desired compaction degree; and (5) repeating the above steps until the predetermined height is reached. The filling project began on 6 July 2018 and ended on 13 May 2019, according to the construction log. There were 30 layers of landfill from 6 July 2018 to 15 September 2018 (Figure 1C), 35 layers from 11 October 2018 to 14 November 2018 (Figure 1D), and 28 layers from 12 March 2019 to 13 May 2019 (Figure 1E). The winter break lasted from 14 November 2018 to 12 March 2019. During the winter break, the site experienced little human disturbance, thus reflecting the actual site deformation process. Therefore, large-scale loess deformation can be observed thoroughly via InSAR and internal monitoring.

We employed a UAV to conduct terrain mapping before and after the project to measure the surface change after filling and applied Agisoft PhotoScan to create the Digital Surface Model (DSM) [37]. The maximum landfill is 24.91 m, and the maximum excavation thickness is 17.30 m, according to the DSM differences in Figure 2.

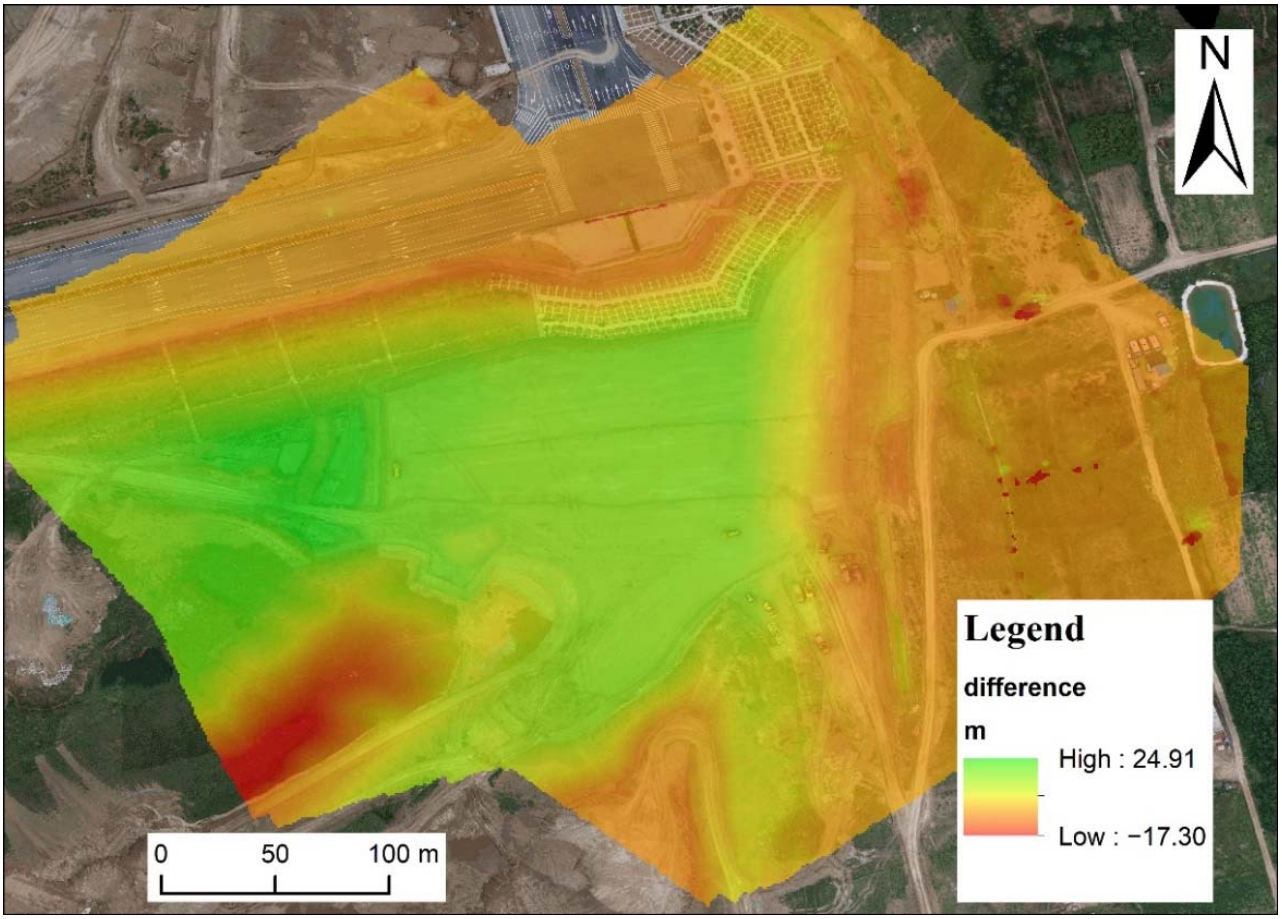

Figure 2. DEM differences before and after filling in the study area (positive value represent filling height and negative values represent excavation depth).

Malan loess is widely distributed in the project area, and the strata are mainly quaternary loose sediments. From the X-ray diffraction, quartz and plagioclase are the main minerals in the Malan loess, which account for 35.2% and 24.0% of minerals, respectively (Table 1). Illite and illite/smectite are the main clay minerals, which account for 41.0% and 35.0% of clays, respectively (Table 2). These characteristics indicate that changes in moisture content can significantly affect the mechanical properties [14,38]. Malan loess is formed by weak cementation between silts, sands, and aggregates. Cementation is provided by crystalline carbonate [39,40]. The Malan loess tensile and shear strengths decrease with water content and increase with dry density, producing a close multi-regression relationship. Differences in tensile strengths between undisturbed loess and remolded loess indicate the significance of its structure [41]. The composition is quaternary alluvial silt, silty clay, sand, and gravel.

Table 1. X-ray diffraction analysis of the relative quantity.

Quartz	Feldspar	Plagioclase	Calcite	Dolomite	Total Clay
35.2	10.9	24.0	11.9	7.6	10.4

Table 2. X-ray diffraction analysis of the relative quantity of clay minerals.

Illite/Smectite	Illite	Kaolinite	Chlorites
41.0	35.0	10.0	14.0

In the study area, we take soil samples and determine the basic parameters in the laboratory (Table 3). According to British Standard (BS 1377) [42], we measured the basic physical property parameters of the samples, while according to the measured volume and mass, the bulk density is 2.03 g/cm^3 for remolded loess, while the density is 1.31 g/cm^3 for undisturbed loess. Subsequently, the samples were dried in an oven until the mass no longer changed (the oven temperature was set to 108 °C). The dry densities of the undisturbed loess and the remolded loess were 1.20 g/cm^3 and 1.80 g/cm^3, and the moisture content was 8.90% and 14.50%. The specific gravity of the loess sample measured by the pycnometer was 2.73. To obtain the void ratio, the equation as follows:

$$e = \frac{(1+\omega)Gs\rho_w}{\rho} - 1 \quad (1)$$

where ω is moisture content, ρ is density, ρ_w is water density, and Gs is specific gravity. Based on the Equation (1), the void ratios of undisturbed loess and remodeled loess are 1.27 and 0.54, respectively. The properties of the loess in the filling area are significantly different from those of the original mountain. These differences in basic properties may result in different deformation characteristics after filling.

Table 3. The basic parameters of the loess in the study area measured by laboratory tests.

Type	Remolded Loess	Undisturbed Loess
Specific gravity	2.73	2.73
Bulk density (g/cm^3)	2.03	1.31
Water content (%)	14.50	8.90
Dry density (g/cm^3)	1.80	1.20
Void ratio	0.54	1.27

3. Methods

3.1. InSAR Process

D-InSAR (differential interferometric synthetic aperture radar) is a technique for mapping ground deformation in the wave phase between two radar images acquired at different times over the same area [43]. PS-InSAR is based on using permanent scatterers to overcome phase decorrelation and atmospheric delay effects in D-InSAR to obtain accurate deformation estimates [44]. Ferretti et al. described the PS-InSAR technique in detail [45]. In the persistent scatterer (PS) targets, the phase includes the deformation phase, atmospheric delay phase, orbit error phase, topographic phase and noise phase as follows:

$$\phi_{int} = \mathrm{W}\left\{\phi_{defo} + \phi_{atmos} + \Delta\phi_{orbit} + \Delta\phi_{topo} + \phi_{noise}\right\} \quad (2)$$

where ϕ_{defo} is the deformation phase, ϕ_{atmos} is the atmospheric delay phase, $\Delta\phi_{orbit}$ is the orbit error phase, $\Delta\phi_{topo}$ is the topographic phase, and ϕ_{noise} is the noise phase. The PS-InSAR method used regression and filtering methods to obtain the real deformation phase.

To date, PS-InSAR has been widely developed. There are many programs for PS-InSAR, such as GAMMA-rs [46], SARPROZ [47], and StaMPS [48]. StaMPS is a software package that allows for the extraction of ground displacements from the time series of synthetic aperture radar (SAR) acquisitions [49,50]. StaMPS applies phase analysis and amplitude to determine the PS probability and calculate displacements on these PSs from the time series of synthetic aperture radar (SAR) acquisitions [44], which it separates into eight steps (Figure 3): (1) data load; (2) phase noise estimation; (3) PS point selection; (4) PS weeding; (5) phase correction; (6) phase unwrapping; (7) estimation of spatially correlated look angle error; and (8) atmosphere filtering [51]. The mean velocity and displacement on each line of sight (*LOS*) can be calculated by StaMPS. Based on the results calculated by StaMPS, we applied our 2-D decomposition method to calculate the displacements.

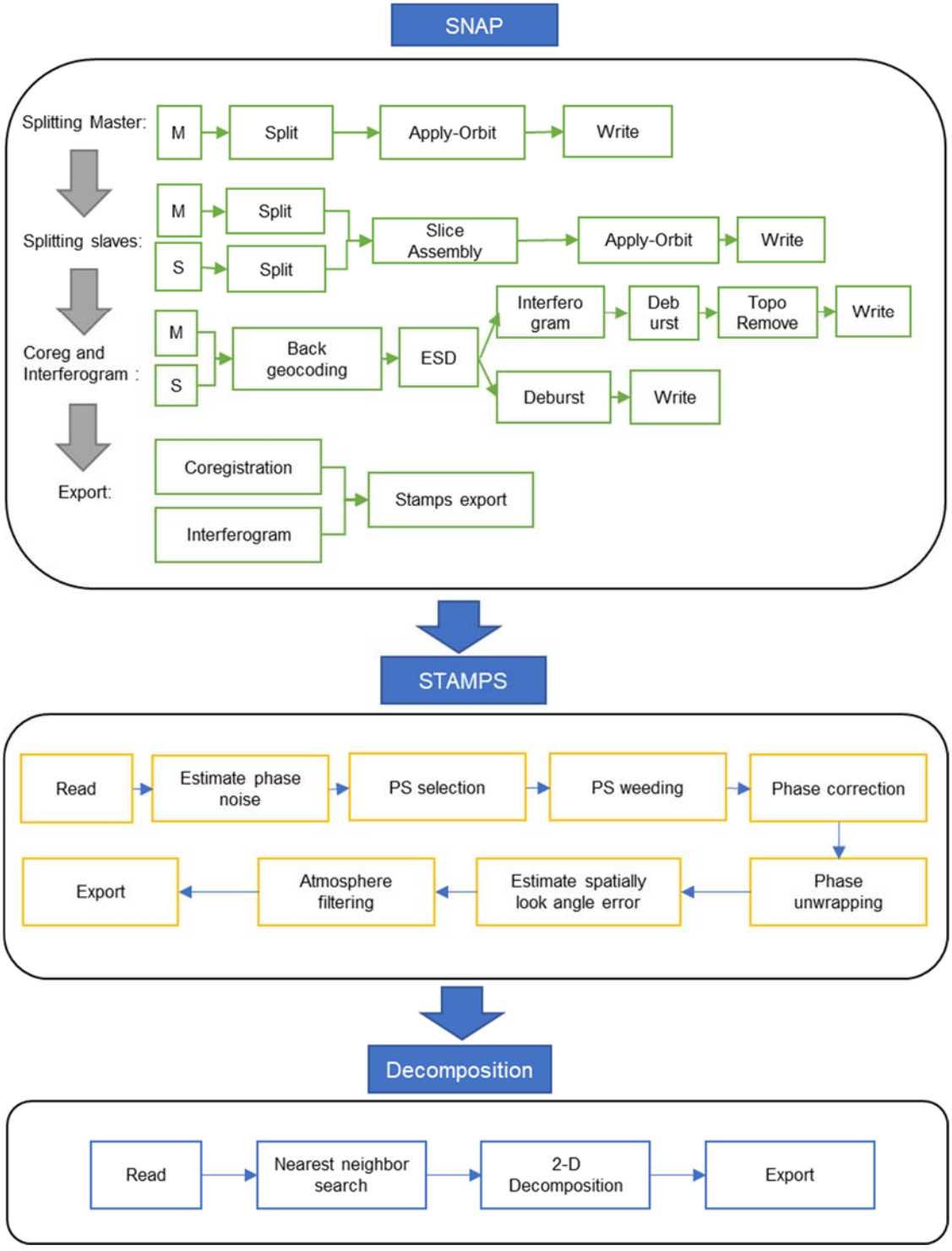

Figure 3. Workflow chart of InSAR.

Sentinel-1 SAR products are free and open access, providing a large number of images to observe deformation around the world. Sentinel Application Platform (SNAP) is the official software for dealing with Sentinel-1 data, which involves coregistration images and the generation of interferograms for data preparation. To integrate SNAP with StaMPS, a free application called snap2stamps [52] was developed and is available on GitHub (https://github.com/mdelgadoblasco/snap2stamps, accessed on 9 May 2022). The workflow for the SNAP–StaMPS approach is shown in Figure 3. In this paper, we used the above method

to deal with the ascending and descending images separately to acquire the deformation on each line of sight (*LOS*) and decomposed them into horizontal and vertical displacements.

3.2. 2-D Decomposition

Based on StaMPS, we can obtain the mean velocity and displacement on each line of sight (*LOS*) through ascending and descending tracks of Sentinel-1 images. SAR is sensitive in the direction perpendicular to its azimuth. Since the Sentinel 1 satellite is in a near-north–south motion, we can obtain the mean velocities and displacements in the vertical and east–west directions based on the ascending and descending images [53–58]. According to the rotation matrix, the east–west motion and vertical motion can be decomposed as follows:

$$\begin{bmatrix} d_{LOS}^{asc} \\ d_{LOS}^{desc} \end{bmatrix} = \begin{bmatrix} \cos\theta_{asc} & -\cos\alpha^{asc}\sin\theta_{asc} \\ \cos\theta_{desc} & -\cos\alpha^{desc}\sin\theta_{desc} \end{bmatrix} \begin{bmatrix} d_v \\ d_e \end{bmatrix} \quad (3)$$

In Equation (3), d_{LOS}^{asc} is the displacement or velocity on the line-of-sight of ascending images, and d_{LOS}^{desc} is the displacement or velocity on the line-of-sight of descending images.

However, the PS in the ascending satellite image and the descending image may not be the same location. Therefore, we cannot decompose the phase on the same PSs. We can assume that the deformation changes in the near region are similar. Then, we estimated the phase and uncertainties according to the PS around the reference and adopted the least squares method. The *LOS* displacement of the ascending and descending images should be included at the same time to prevent equation collinearity (Figure 4). Equation (3) changes to:

$$Y = AX \quad (4)$$

where $X = \begin{bmatrix} d_v \\ d_e \end{bmatrix}$, $Y = \left[d_{LOS_1{}^{asc}}, \ldots, d_{LOS_n{}^{asc}}, d_{LOS_1{}^{desc}}, \ldots, d_{LOS_m{}^{desc}} \right]^T$, and A is:

$$\begin{bmatrix} \cos\theta_1{}^{asc} & \cdots & \cos\theta_n{}^{asc} & \cos\theta_1{}^{desc} & \cdots & \cos\theta_m{}^{desc} \\ -\cos\alpha^{asc}\sin\theta_1{}^{asc} & \cdots & -\cos\alpha^{asc}\sin\theta_n{}^{asc} & -\cos\alpha^{desc}\sin\theta_1{}^{desc} & \cdots & -\cos\alpha^{\mathrm{desc}}\sin\theta_m{}^{desc} \end{bmatrix}^T$$

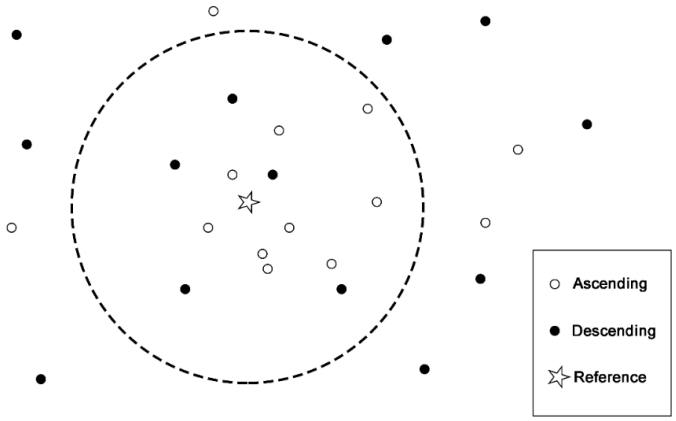

Figure 4. The selection of the PS correction point in the reference PS points.

θ_i^{asc} is the radar incidence angle at the ith PS point through the ascending tracks of Sentinel-1 images, θ_j^{desc} is the radar incidence angle at the jth PS point through the descending tracks of Sentinel-1 images, α^{asc} is the *LOS* azimuth on the ascending tracks, α^{desc} is the *LOS* azimuth on the descending tracks, $d_{LOS^{asc}}$ is the displacement or velocities along the line-of-sight (*LOS*) through the ascending tracks of Sentinel-1 images, $d_{LOS^{desc}}$ is the displacement or velocity along the line-of-sight (*LOS*) through the ascending tracks of the Sentinel-1 images, d_v is the vertical displacement or velocity, and d_e is the displacement or velocity in the east–west direction. Based on the least squares method, X is:

$$X = \left(A^T A\right)^{-1} A^T Y \quad (5)$$

For each PS, we can calculate the east–west displacement and vertical displacement and velocity according to the above method.

3.3. Field Monitoring

We buried instruments in the soil layers to monitor vertical and horizontal stress, deformation, and moisture movements. Three earth pressure cells were buried in this area: two earth pressure cells monitored the horizontal pressure, and one monitored the vertical pressure. Two earth pressure cells were in the landfill at 16 m and 19.4 m relative to the designed elevation to monitor the horizontal pressure. One earth pressure cell was placed at the bottom interface (21 m relative to the designed elevation) to monitor the vertical pressure. For deformation, three extensometers were used to monitor the deformation: two for horizontal deformation and one for vertical deformation. For horizontal deformation, we monitored deformations in the filling area and boundary area. For vertical deformation, the meter monitors the deformation from 16 m to 21 m relative to the designed elevation. For the moisture movement, two moisture meters were located in the filling areas and excavation areas. The schematic layout of the equipment is shown in Figure 5. According to the above monitoring equipment data, the deformation process of the internal landfill area can be measured.

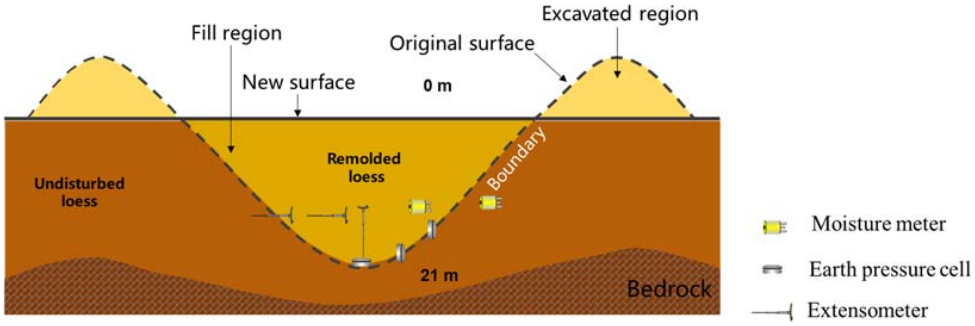

Figure 5. Schematic diagram of buried equipment layout.

4. Results

4.1. Surface Monitoring

Considering Sentinel 1 satellite imagery coverage, we selected nine ascending and nine descending images of this area on the same day during the winter break from 29 November 2018 to 5 March 2019 (Table 4). Then, we adopted the above method to calculate the surface deformation in the vertical and east–west directions. In our method, a positive value in the east–west direction indicates western movement and a positive value in the vertical direction indicates uplift after decomposition.

Table 4. Sentinel data for the LNA.

Ascending		Descending	
No.	**Acquisition Date**	**No.**	**Acquisition Date**
1	29 November 2018	1	29 November 2018
2	11 December 2018	2	11 December 2018
3	23 December 2018	3	23 December 2018
4	4 January 2019	4	4 January 2019
5	16 January 2019	5	16 January 2019
6	28 January 2019	6	28 January 2019
7	9 February 2019	7	9 February 2019
8	21 February 2019	8	21 February 2019
9	5 March 2019	9	5 March 2019

According to the spatial distribution of PS points, they are distributed in the original mountain and cutting areas. There are few PS points in the filling area due to rapid settlement (Figure 6A); therefore, in situ monitoring is required.

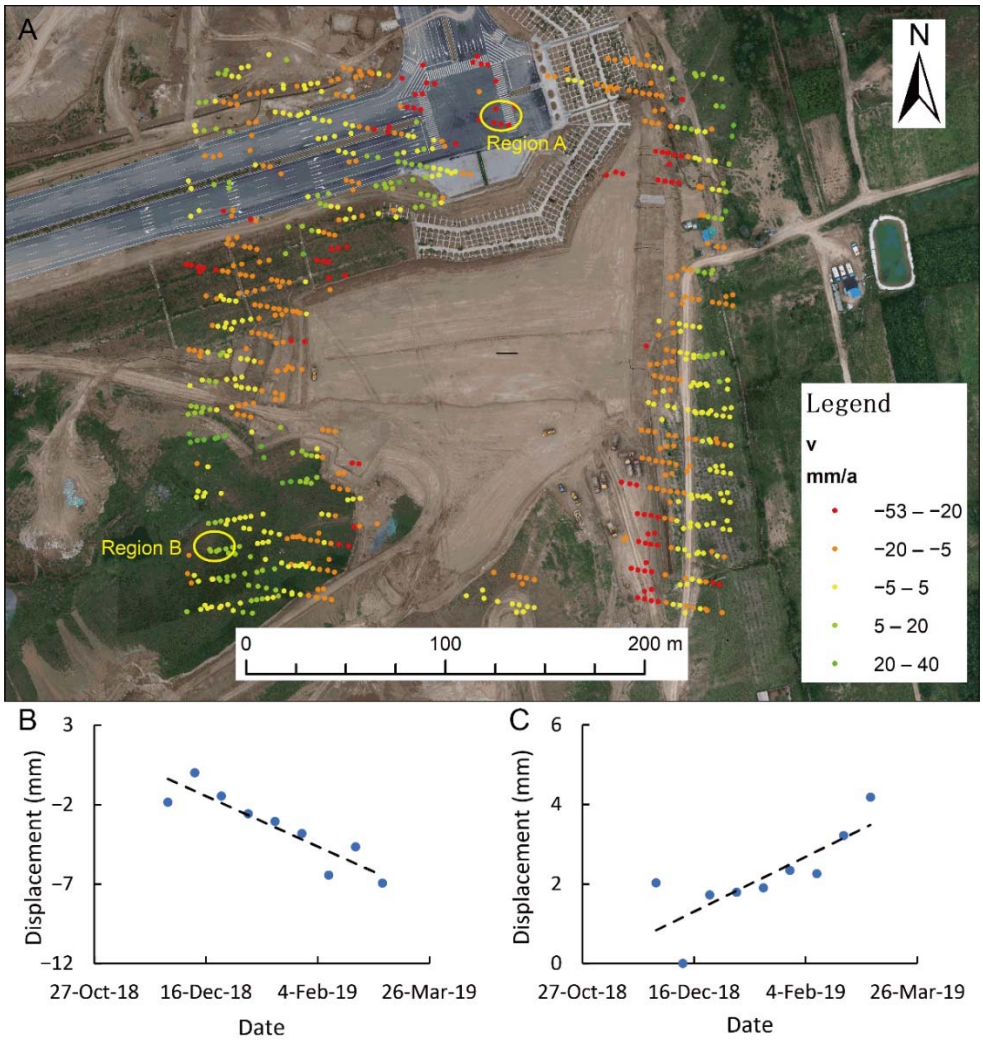

Figure 6. The vertical deformation based on InSAR data ((**A**) is the spatial distribution of vertical deformation, (**B**) is the deformation in region A, and (**C**) is the deformation in region B).

The characteristics of deformation in different areas are different. On the road, there is heterogeneity. There is significant settlement in region A (Figure 6B); however, there is an uplift in the excavation area (Figure 6C) throughout the winter break. The settlement in region A in Figure 6A appears to be more than 20 mm/year, which is affected by the filling projects. In the excavation area, the deformation rate is greater than 5 mm per year, which is related to the cutting process.

According to the horizontal deformation, the movements in the east–west direction show different deformations in the boundary areas and the excavation areas (Figure 7A). Different boundaries show different deformation characteristics. The eastern boundaries (Region A in Figure 7A), i.e., high-fill boundaries, appear to have moved eastwards due to the absence of the original mountain restrictions (>20 mm/a) (Figure 7B), while deformation is relatively low at the western boundary. Additionally, the excavation area appeared to move west (Region B in Figure 7A). The velocity of the excavation area is more than 10 mm/year (Figure 7C). Therefore, the filling procedure will have an impact on the neighboring areas based on these InSAR observations.

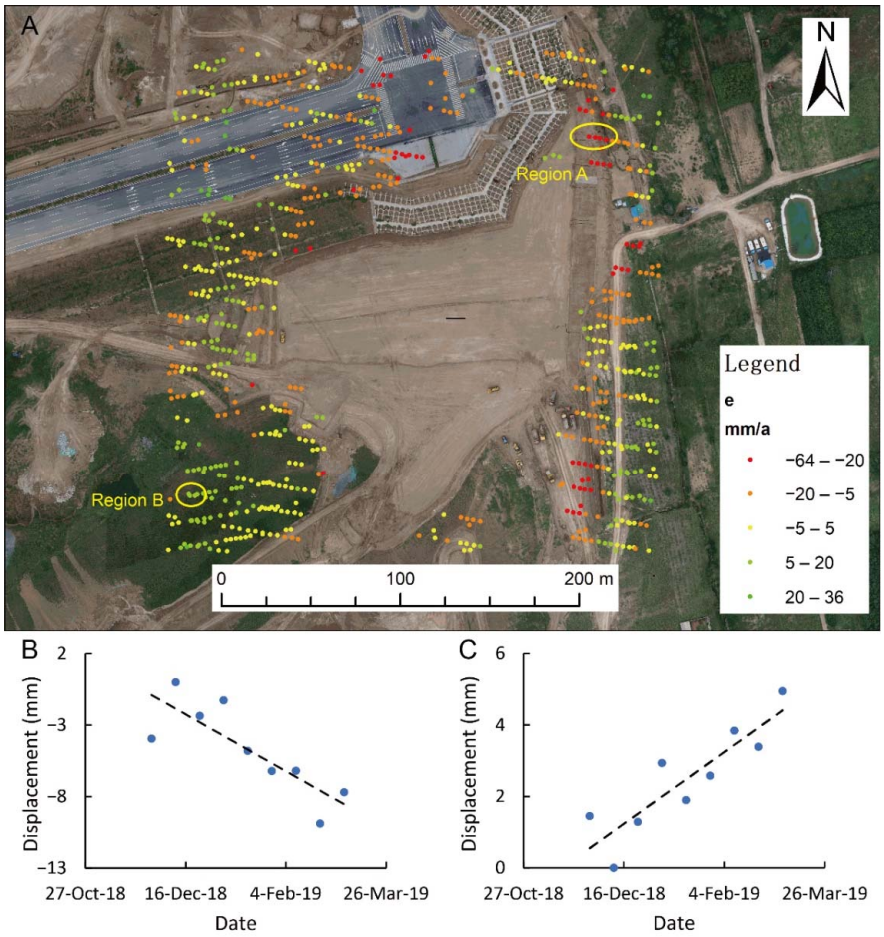

Figure 7. East–west displacement based on InSAR data ((**A**) is the spatial distribution of displacement in the east–west direction, (**B**) is the deformation in region A, and (**C**) is the deformation in region B).

4.2. Internal Monitoring

The geological body is composed of undisturbed loess and remolded loess, which results in complex deformation processes [59]. Based on field monitoring, the deformations during construction are large and range from 16 m to 21 m during the filling process (Figure 8). The pressure at 21 m presents an increase in the filling process (Figure 8A); this pressure is from 125.3 kPa to 172.3 kPa during construction (about 2.14 kPa/day). In terms of vertical deformation, it is about −10.3 mm, and the average velocity is about 0.47 mm/day during construction (Figure 8B).

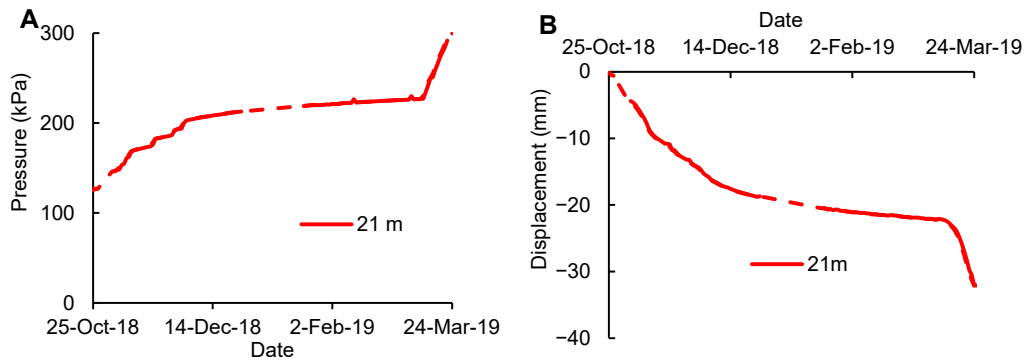

Figure 8. Vertical stress at 21 m and displacement from 16 m to 21 m in the filling areas in the first stage ((**A**) is the pressure over time, and (**B**) is the displacement over time. The solid line is the measured data, and the dashed line is the estimation of missing data due to a lack of data).

During the winter break, the pressure ranged from 172.3 kPa to 227.1 kPa. This process shows that stress in the filling bodies is redistributed (Figure 9A). In addition, the settlement reaches 12 mm from 16 m to 21 m (Figure 9B). The relationship between settlement and time follows logarithmic models during the winter down period, similar to previous studies [60–62].

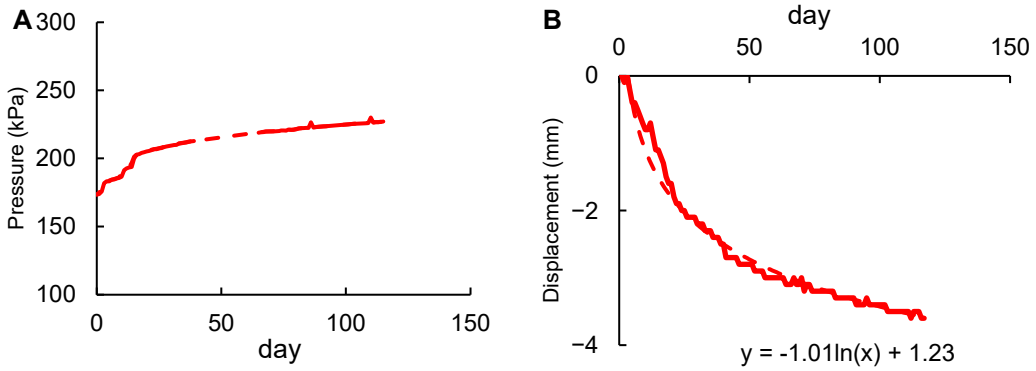

Figure 9. Vertical stress at 21 m and displacement from 16 m to 21 m in the filling areas during winter break ((**A**) is the pressure over time during winter, and (**B**) is the displacement over time during winter. The solid line is the measured data, and the dashed line is the estimation of missing data due to a lack of data).

Compared with vertical deformation, the horizontal deformation is complicated [59]. The horizontal deformation in different areas presents different characteristics: the loess is tense in the filling area and compressed at the boundary (Figure 10A,B). Based on the data measured by the horizontal displacement gauge, the horizontal displacement increased by approximately 2.5 mm in the filling area and decreased by 1 mm at the boundary from 25 October 2018 to 24 March 2019 (Figure 10C). The lateral stress increased rapidly during construction and grew slowly during the winter break (Figure 11). At the same time, this process shows that the filling area is not stable during the winter break. Additionally, the high strength when the undisturbed loess is dry prevents the disturbed loess from moving due to the mechanical characteristics. The results show that the filling body will affect the adjacent areas. According to the above analysis, the internal monitoring results are in good agreement with the surface InSAR measurements. These results show that the filling bodies may squeeze surrounding areas.

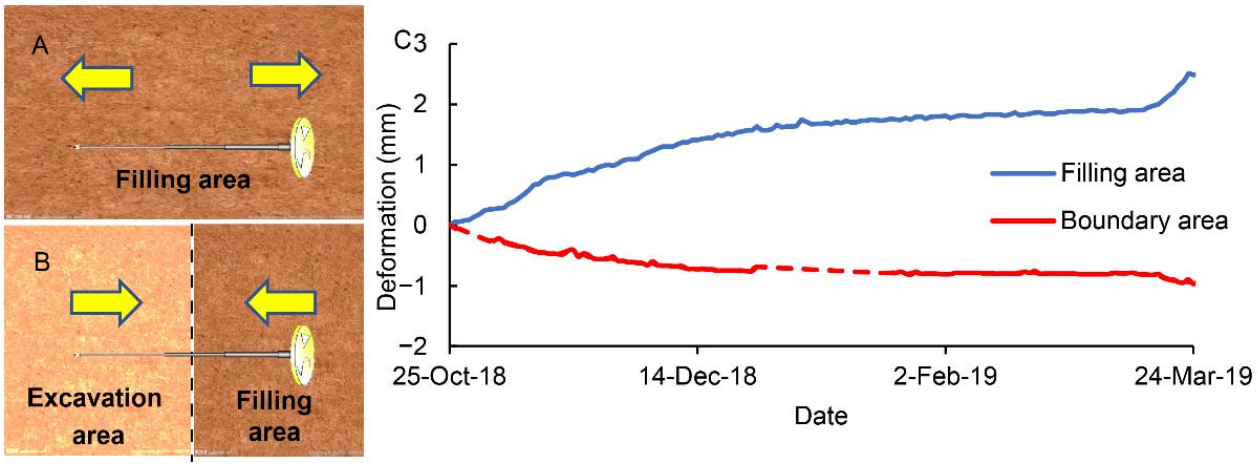

Figure 10. Horizontal displacement ((**A**) is a schematic diagram of the deformation of the landfill area, (**B**) is a schematic diagram of the deformation at the boundary, and (**C**) is the deformation over time).

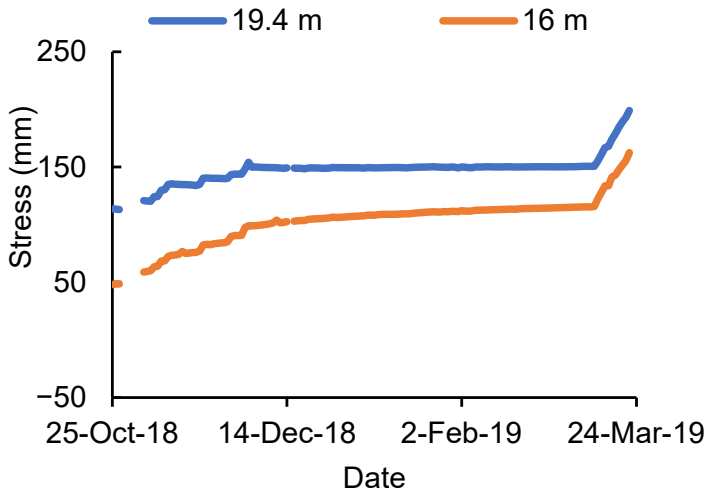

Figure 11. Horizontal stresses (the blue line is at 19.4 m, and the orange line is at 16 m).

5. Discussion

5.1. Effects of Different Compressibilities

The compression tests were conducted on a one-dimensional oedometer apparatus at the College of Geological Engineering and Geomatics, Chang'an University. The Accuracy of this equipment is ±0.001 mm. In this test, we set the pressure to 12.5 kPa, 25 kPa, 50 kPa, 100 kPa, 200 kPa, 400 kPa, 600 kPa, 800 kPa, 1600 kPa, and 3200 kPa on the in situ remolded and undisturbed loess. At each loading step, the settlement of the specimens was measured so that the void ratio could be calculated.

Regarding the results, there are some differences in the compressibility between undisturbed loess and remolded loess (Figure 12). The coefficient of compressibility in undisturbed loess decreases from 0.78 MPa^{-1} to 0.07 MPa^{-1}. For the remolded loess, the curve decreases linearly with pressure in the e-logp plot (Figure 12). The coefficient of compressibility is 1.13 MPa^{-1}, and it gradually decreases to 0.02 MPa^{-1}. Before the load reaches a certain threshold, the compression deformation of undisturbed loess is relatively small, and the compression curve of undisturbed loess is gentler than that of remolded loess. However, when the load exceeds the threshold, the void ratio decreases rapidly. The compression curve of the undisturbed soil after the load exceeds the threshold is steeper than that of the remolded loess, and the compression index of the undisturbed loess is larger than that of the remolded loess. Undisturbed loess has more pores, which provides room for compression. With increasing pressure, the structure of undisturbed loess gradually began to play a role, and the changes in the two curves were also significantly different.

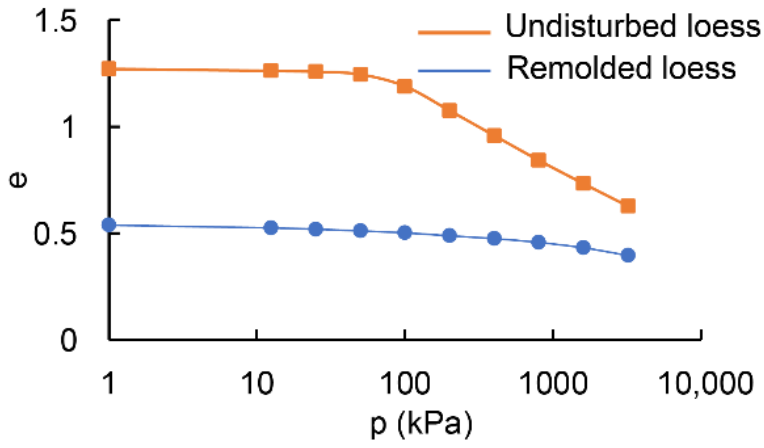

Figure 12. Compression curve shown by *e*-log*p* plots (the orange line is undisturbed loess, and the blue line is remolded loess).

In the filling project, due to the difference in compressibility, the internal deformation of loess produces different characteristics. The compression of undisturbed loess is small compared with that of remolded loess under low pressure. These differences cause the border to appear compressed. The filling body squeezes the adjacent areas. Therefore, different compression properties are one of the reasons that the boundary area becomes a vital area of loess.

5.2. Effects of Different Permeabilities

The volumetric water content (VWC) shows an increasing trend on both sides of the boundary. The process may be related to the groundwater level rising during the filling process. However, there are differences in volumetric water content on both sides of the boundary (Figure 13). According to laboratory tests for in situ loess, remolded loess and undisturbed loess have different hydraulic conductivities: 2.3×10^{-5} m/s for remolded loess and 1.4×10^{-4} m/s for undisturbed loess (Table 5). The hydraulic conductivity of undisturbed loess is an order of magnitude higher than that of remolded loess, which may induce different moisture movements. The difference in the soil properties may lead to different transport processes and cause different moisture concentrations at the boundary [63]. Therefore, the difference in horizontal deformation is related to moisture. In particular, these hydraulic discontinuities may contribute to high pore pressures during intense rainstorms and loading. In the filling project, moisture movement affects the high-fill slope stability, which causes settlement [64].

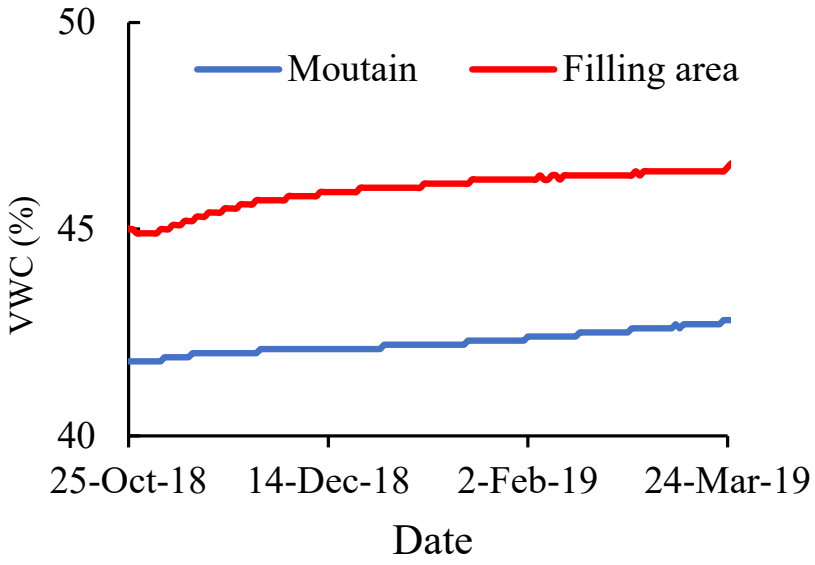

Figure 13. VWC on both sides of the boundary (the blue line is VWC in the original mountain, and the red line is VWC in the filling area).

Table 5. Permeability coefficients of undisturbed loess and remolded loess.

Type of Loess	Sample	Permeability Coefficient	Average Permeability Coefficient
Remolded loess	F01	2.6×10^{-5} m/s	2.3×10^{-5} m/s
	F02	2.2×10^{-5} m/s	
	F03	2.1×10^{-5} m/s	
Undisturbed loess	W01	1.5×10^{-4} m/s	1.4×10^{-4} m/s
	W02	1.4×10^{-4} m/s	
	W03	1.3×10^{-4} m/s	

Based on the above monitoring data, the filling process affects adjacent areas due to having different physical properties and different water contents. The deformation char-

acteristics affected by various factors are not homogeneous. The InSAR results show that the high filling boundary moves outward under the force of gravity. Internal monitoring shows that the boundary region shows a state of compression, while the landfill region shows a state of expansion.

5.3. Lessons from Monitoring

The project has provided new flat land for local agriculture and promoted economic development (Figure 14). This study demonstrates the early deformation characteristics of loess landfill through an air–space–ground integrated monitoring technique. In the excavation area, the deformation characteristics are similar to those of the core of LNA, which uplifts slightly. In the filling areas, due to soil instability in the landfill area, there are few PS points, so it is impossible to measure the deformation through InSAR accurately. From the vertical displacement meter in the filling body, the deformation from 16 m to 21 m reaches about 37.12 mm/a. However, the maximum annual deformation rate in the urban core areas of LNA measured by InSAR was 56.35 mm/a [34]. There are two main reasons for the difference in settlement: (1) different landfill methods and (2) different settling time intervals. Firstly, the study area has only just been landfilled, and the subsidence is relatively fast. In addition, due to this leveled land being intended for agriculture, roller compaction was selected for the landfill process. In general, the deformation in this area after the landfill process is within expectations. In addition, pressure and deformation are related to the filling process. The pressure and deformation increased following the filling process. However, the deformation and stress have some hysteresis according to the monitoring data.

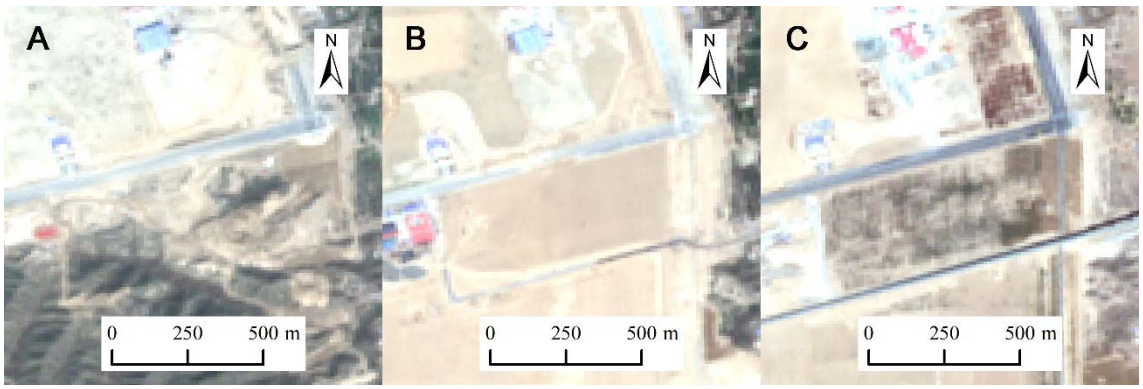

Figure 14. Changes in the research area ((**A**) is on 12 October 2018; (**B**) is on 4 July 2019; (**C**) is on 4 May 2022).

As a result of urban development, filling projects are distributed widely around the world, including projects such as Kansai International Airport in Japan [65], Macau International Airport in China [66], and Treasure Island in the USA [67]. Unreasonable landfill methods may cause geological disasters such as the Shenzhen landslide. Additionally, land subsidence is one of the problems in these areas. This case shows that we can use different landfill methods depending on the purposes and costs. It is also necessary to install monitoring equipment to monitor deformation. When abnormal deformations appear, we should take measures to control them.

6. Conclusions

In this study, we monitored large-scale deformation and investigated the causes using large-scale field monitoring from Sentinel-1 satellite data, in situ monitoring equipment, and laboratory tests. The following conclusions can be drawn:

(1) During the construction, stress and deformation increase rapidly (2.14 kPa/day for vertical stress at 21 m relative to the designed elevation and 0.47 mm/day from 16 m

to 21 m relative to the designed elevation). The loess in the filling area is the state of expansion while the state of compression is at the boundary. The deformation and stress have some hysteresis;

(2) During winter, the deformations in different regions varied. In the horizontal direction, the excavation area exhibits horizontal movement. Some boundaries appear to cause extrusion deformation in adjacent regions. The high filling boundary moves outward under the force of gravity (the deformation velocity in some areas exceeds 20 mm/a). In the vertical direction, there is an uplift in excavated areas and subsidence in the fill region;

(3) The water content on both sides of the boundary gradually increases due to the influence of the filling project. Different permeability properties indicate that the boundary area is critical. The filling and excavation processes have impacted the surrounding area;

(4) The compression characteristics of undisturbed loess and remolded loess are different, which is one of the reasons for their different deformation characteristics. At low pressure, the compressibility coefficient of undisturbed loess (0.78 MPa^{-1}) is lower than that of remolded loess (1.13 MPa^{-1}), but at high pressure, the compressibility coefficient of undisturbed loess (0.07 MPa^{-1}) is higher than that of remolded loess (0.02 MPa^{-1}). Different mechanical properties and hydraulic conductivities may trigger differential soil transfer and cause geohazards. It is also necessary to install monitoring equipment to monitor deformation. When abnormal deformations appear, measures should be taken to control them.

Author Contributions: Conceptualization, Y.W. and H.L.; methodology, Y.W.; validation, Y.W.; formal analysis, Y.W.; investigation, H.L.; resources, H.L.; writing—original draft preparation, Y.W.; writing—review and editing, H.L.; supervision, H.L.; project administration, H.L.; funding acquisition, H.L. All authors have read and agreed to the published version of the manuscript.

Funding: This study was supported by the National Natural Science Foundation of China (Grant NO. 41927806, 42041006 and 41790443) and the Strategic Priority Research Program of the Chinese Academy of Sciences (CAS) (Grant NO. XDA23090301).

Institutional Review Board Statement: Not applicable.

Informed Consent Statement: Not applicable.

Data Availability Statement: Not applicable.

Acknowledgments: We thank Chen Junhui, Lin Gan, and Tian Zhaoyang for burying the equipment and giving their suggestions regarding this paper.

Conflicts of Interest: The authors declare no conflict of interest.

References

1. Li, Y.; Yang, J.; Hu, X. Origin of ground fissures in the Shanxi Graben System, Northern China. *Eng. Geol.* **2000**, *55*, 267–275. [CrossRef]
2. Juang, C.H.; Dijkstra, T.; Wasowski, J.; Meng, X. Loess geohazards research in China: Advances and challenges for mega engineering projects. *Eng. Geol.* **2019**, *251*, 1–10. [CrossRef]
3. Peng, J.; Qi, S.; Williams, A.; Dijkstra, T.A. Preface to the special issue on "Loess engineering properties and loess geohazards". *Eng. Geol.* **2018**, *236*, 1–3. [CrossRef]
4. Li, Y.; Li, Y.; Fang, B.; Qu, L.; Wang, C.; Li, W. Land use change and farmers' sense of place in typical catchment of the Loess hilly and gully region of China. *Land* **2021**, *10*, 810. [CrossRef]
5. Chen, G.; Zhang, Y.; Zeng, R.; Yang, Z.; Chen, X.; Zhao, F.; Meng, X. Detection of Land Subsidence Associated with Land Creation and Rapid Urbanization in the Chinese Loess Plateau Using Time Series InSAR: A Case Study of Lanzhou New District. *Remote Sens.* **2018**, *10*, 270. [CrossRef]
6. Li, P.; Qian, H.; Wu, J. Environment: Accelerate research on land creation. *Nature* **2014**, *510*, 29–31. [CrossRef]
7. Niu, Q.; Bai, J.; Cheng, W.; Dang, X.; Wang, G.; Gao, X.; Wang, Y. Mapping the dynamics of urban land creation from hilltop removing and gully filling Projects in the river-valley city of Lanzhou, China. *J. Indian Soc. Remote Sens.* **2022**, 1–14. [CrossRef]
8. Liu, Y.; Li, Y. China's land creation project stands firm. *Nature* **2014**, *511*, 410. [CrossRef]

9. Jin, Z. The creation of farmland by gully filling on the Loess Plateau: A double-edged sword. *Environ. Sci. Technol.* **2014**, *48*, 883–884. [CrossRef]
10. Assallay, A.M.; Rogers, C.D.F.; Smalley, I.J. Formation and collapse of metastable particle packings and open structures in loess deposits. *Eng. Geol.* **1997**, *48*, 101–115. [CrossRef]
11. Barden, L.; McGown, A.; Collins, K. The collapse mechanism in partly saturated soil. *Eng. Geol.* **1973**, *7*, 49–60. [CrossRef]
12. Dijkstra, T.A.; Smalley, I.J.; Rogers, C.D.F. Particle packing in loess deposits and the problem of structure collapse and hydroconsolidation. *Eng. Geol.* **1995**, *40*, 49–64. [CrossRef]
13. Li, P.; Qian, H. Water in loess. In *Encyclopedia of Sustainability Science and Technology*; Springer: New York, NY, USA, 2018; pp. 1–17.
14. Wen, B.-P.; Yan, Y.-J. Influence of structure on shear characteristics of the unsaturated loess in Lanzhou, China. *Eng. Geol.* **2014**, *168*, 46–58. [CrossRef]
15. Derbyshire, E.; Dijkstra, T.A.; Smalley, I.J.; Li, Y. Failure mechanisms in loess and the effects of moisture content changes on remoulded strength. *Quat. Int.* **1994**, *24*, 5–15. [CrossRef]
16. Lutenegger, A.J.; Hallberg, G.R. Stability of loess. *Eng. Geol.* **1988**, *25*, 247–261. [CrossRef]
17. Yao, Y.; Wang, R.; Yang, J.; Yue, P.; Lu, D.; Xiao, G.; Wang, Y.; Liu, L. Changes in terrestrial surface dry and wet conditions on the Loess Plateau (China) during the last half century. *J. Arid Land* **2013**, *5*, 15–24. [CrossRef]
18. Meng, X.; Liao, H.; Zhang, J. Infiltration law of water in undisturbed loess and backfill. *Water* **2020**, *12*, 2388. [CrossRef]
19. Fredlund, D.; Gan, J. The collapse mechanism of a soil subjected to one-dimensional loading and wetting. In *Genesis and Properties of Collapsible Soils*; Springer: Dordrecht, The Netherlands, 1995; pp. 173–205.
20. Dexter, A.R.; Tanner, D.W. Time Dependence of Compressibility for Remoulded and Undisturbed Soils. *J. Soil Sci.* **1974**, *25*, 153–164. [CrossRef]
21. Shao, S.J.; She, F.T.; Fang, J. Mechanical Behavior of Segmented Lining Structure of Tunnel under Acting Ground Fractures in Xi'an Zone. *Adv. Mater. Res.* **2011**, *261–263*, 1778–1783. [CrossRef]
22. Jiang, M.; Zhang, F.; Hu, H.; Cui, Y.; Peng, J. Structural characterization of natural loess and remolded loess under triaxial tests. *Eng. Geol.* **2014**, *181*, 249–260. [CrossRef]
23. Miao, F.; Wu, Y.; Török, Á.; Li, L.; Xue, Y. Centrifugal model test on a riverine landslide in the Three Gorges Reservoir induced by rainfall and water level fluctuation. *Geosci. Front.* **2022**, *13*, 101378. [CrossRef]
24. Miao, F.; Wu, Y.; Xie, Y.; Li, Y. Prediction of landslide displacement with step-like behavior based on multialgorithm optimization and a support vector regression model. *Landslides* **2018**, *15*, 475–488. [CrossRef]
25. Liu, X.; Zhao, C.; Zhang, Q.; Peng, J.; Zhu, W.; Lu, Z. Multi-Temporal Loess Landslide Inventory Mapping with C-, X- and L-Band SAR Datasets—A Case Study of Heifangtai Loess Landslides, China. *Remote Sens.* **2018**, *10*, 1756. [CrossRef]
26. Shi, X.; Yang, C.; Zhang, L.; Jiang, H.; Liao, M.; Zhang, L.; Liu, X. Mapping and characterizing displacements of active loess slopes along the upstream Yellow River with multi-temporal InSAR datasets. *Sci. Total Environ.* **2019**, *674*, 200–210. [CrossRef]
27. Gray, L. Using multiple RADARSAT InSAR pairs to estimate a full three-dimensional solution for glacial ice movement. *Geophys. Res. Lett.* **2011**, *38*, L05502. [CrossRef]
28. Chen, B.; Gong, H.; Li, X.; Lei, K.; Zhu, L.; Gao, M.; Zhou, C. Characterization and causes of land subsidence in Beijing, China. *Int. J. Remote Sens.* **2017**, *38*, 808–826. [CrossRef]
29. Schlögel, R.; Doubre, C.; Malet, J.-P.; Masson, F. Landslide deformation monitoring with ALOS/PALSAR imagery: A D-InSAR geomorphological interpretation method. *Geomorphology* **2015**, *231*, 314–330. [CrossRef]
30. Zhao, C.; Zhang, Q.; He, Y.; Peng, J.; Yang, C.; Kang, Y. Small-scale loess landslide monitoring with small baseline subsets interferometric synthetic aperture radar technique—Case study of Xingyuan landslide, Shaanxi, China. *J. Appl. Remote Sens.* **2016**, *10*, 026030. [CrossRef]
31. Xue, Y.T.; Meng, X.M.; Li, K.; Chen, G. Loess Slope Instability Assessment Based on PS-InSAR Detected and Spatial Analysis in Lanzhou Region, China. *Adv. Mater. Res.* **2014**, *1065–1069*, 2342–2352. [CrossRef]
32. Zeng, R.Q.; Meng, X.M.; Wasowski, J.; Dijkstra, T.; Bovenga, F.; Xue, Y.T.; Wang, S.Y. Ground instability detection using PS-InSAR in Lanzhou, China. *Q. J. Eng. Geol. Hydrogeol.* **2014**, *47*, 307–321. [CrossRef]
33. Hu, X.; Xue, L.; Yu, Y.; Guo, S.; Cui, Y.; Li, Y.; Qi, S. Remote Sensing Characterization of Mountain Excavation and City Construction in Loess Plateau. *Geophys. Res. Lett.* **2021**, *48*, e2021GL095230. [CrossRef]
34. He, Y.; Chen, Y.; Wang, W.; Yan, H.; Zhang, L.; Liu, T. TS-InSAR analysis for monitoring ground deformation in Lanzhou New District, the loess Plateau of China, from 2017 to 2019. *Adv. Space Res.* **2021**, *67*, 1267–1283. [CrossRef]
35. Wei, Y.; Liu, X.; Zhao, C.; Tomás, R.; Jiang, Z. Observation of Surface Displacement Associated with Rapid Urbanization and Land Creation in Lanzhou, Loess Plateau of China with Sentinel-1 SAR Imagery. *Remote Sens.* **2021**, *13*, 3472. [CrossRef]
36. Wu, Q.; Jia, C.; Chen, S.; Li, H. SBAS-InSAR based deformation detection of urban land, created from mega-scale mountain excavating and valley filling in the Loess Plateau: The case study of Yan'an City. *Remote Sens.* **2019**, *11*, 1673. [CrossRef]
37. Agisoft, L. PhotoScan Python Reference. *Release* **2016**, *1*, 63.
38. Luo, H.; Wu, F.; Chang, J.; Xu, J. Microstructural constraints on geotechnical properties of Malan Loess: A case study from Zhaojiaan landslide in Shaanxi province, China. *Eng. Geol.* **2018**, *236*, 60–69. [CrossRef]
39. Li, Y.; He, S.; Deng, X.; Xu, Y. Characterization of macropore structure of Malan loess in NW China based on 3D pipe models constructed by using computed tomography technology. *J. Asian Earth Sci.* **2018**, *154*, 271–279. [CrossRef]

40. Wei, Y.-N.; Fan, W.; Yu, B.; Deng, L.-S.; Wei, T. Characterization and evolution of three-dimensional microstructure of Malan loess. *Catena* **2020**, *192*, 104585. [CrossRef]
41. Li, Y. A review of shear and tensile strengths of the Malan Loess in China. *Eng. Geol.* **2018**, *236*, 4–10. [CrossRef]
42. Standard, B. *Methods of Test for Soils for Civil Engineering Purposes*; British Standards Institution: London, UK, 1990; BS1377.
43. Botey i Bassols, J.; Vàzquez-Suñé, E.; Crosetto, M.; Barra, A.; Gerard, P. D-InSAR monitoring of ground deformation related to the dewatering of construction sites. A case study of Glòries Square, Barcelona. *Eng. Geol.* **2021**, *286*, 106041. [CrossRef]
44. Sousa, J.J.; Ruiz, A.M.; Hanssen, R.F.; Bastos, L.; Gil, A.J.; Galindo-Zaldívar, J.; de Galdeano, C.S. PS-InSAR processing methodologies in the detection of field surface deformation—Study of the Granada basin (Central Betic Cordilleras, southern Spain). *J. Geodyn.* **2010**, *49*, 181–189. [CrossRef]
45. Ferretti, A.; Prati, C.; Rocca, F. Permanent scatterers in SAR interferometry. *IEEE Trans. Geosci. Remote Sens.* **2001**, *39*, 8–20. [CrossRef]
46. Werner, C.; Wegmüller, U.; Strozzi, T.; Wiesmann, A. Gamma SAR and interferometric processing software. In Proceedings of the Ers-Envisat Symposium, Gothenburg, Sweden, 15–20 October 2000; p. 1620.
47. Perissin, D. SARPROZ Software Manual. 2016. Available online: https://www.sarproz.com (accessed on 12 May 2022).
48. Hooper, A.; Spaans, K.; Bekaert, D.; Cuenca, M.C.; Arıkan, M.; Oyen, A. *StaMPS/MTI Manual*; Delft Institute of Earth Observation and Space Systems Delft University of Technology: Kluyverweg, The Netherlands, 2010; Volume 1, p. 2629.
49. Hooper, A. A multi-temporal InSAR method incorporating both persistent scatterer and small baseline approaches. *Geophys. Res. Lett.* **2008**, *35*, L16302–L16309. [CrossRef]
50. Hooper, A.; Segall, P.; Zebker, H. Persistent scatterer interferometric synthetic aperture radar for crustal deformation analysis, with application to Volcán Alcedo, Galápagos. *J. Geophys. Res. Solid Earth* **2007**, *112*, B07407. [CrossRef]
51. Zhou, S.; Ouyang, C.; Huang, Y. An InSAR and depth-integrated coupled model for potential landslide hazard assessment. *Acta Geotech.* **2022**, *17*, 3613–3632. [CrossRef]
52. Foumelis, M.; Blasco, J.M.D.; Desnos, Y.-L.; Engdahl, M.; Fernández, D.; Veci, L.; Lu, J.; Wong, C. ESA SNAP-StaMPS integrated processing for Sentinel-1 persistent scatterer interferometry. In Proceedings of the IGARSS 2018—2018 IEEE International Geoscience and Remote Sensing Symposium, Valencia, Spain, 4 November 2018; pp. 1364–1367.
53. Bayramov, E.; Buchroithner, M.; Kada, M.; Zhuniskenov, Y. Quantitative Assessment of Vertical and Horizontal Deformations Derived by 3D and 2D Decompositions of InSAR Line-of-Sight Measurements to Supplement Industry Surveillance Programs in the Tengiz Oilfield (Kazakhstan). *Remote Sens.* **2021**, *13*, 2579. [CrossRef]
54. Fuhrmann, T.; Garthwaite, M.C. Resolving three-dimensional surface motion with InSAR: Constraints from multi-geometry data fusion. *Remote Sens.* **2019**, *11*, 241. [CrossRef]
55. Aslan, G.; Cakir, Z.; Lasserre, C.; Renard, F. Investigating subsidence in the Bursa Plain, Turkey, using ascending and descending Sentinel-1 satellite data. *Remote Sens.* **2019**, *11*, 85. [CrossRef]
56. Fialko, Y. Interseismic strain accumulation and the earthquake potential on the southern San Andreas fault system. *Nature* **2006**, *441*, 968–971. [CrossRef]
57. Motagh, M.; Shamshiri, R.; Haghighi, M.H.; Wetzel, H.-U.; Akbari, B.; Nahavandchi, H.; Roessner, S.; Arabi, S. Quantifying groundwater exploitation induced subsidence in the Rafsanjan plain, southeastern Iran, using InSAR time-series and in situ measurements. *Eng. Geol.* **2017**, *218*, 134–151. [CrossRef]
58. Pawluszek-Filipiak, K.; Borkowski, A. Integration of DInSAR and SBAS Techniques to determine mining-related deformations using sentinel-1 data: The case study of Rydułtowy mine in Poland. *Remote Sens.* **2020**, *12*, 242. [CrossRef]
59. Yao, Y.; Zhang, Y.; Ma, C.; Zhao, Y.; Lv, G. Study on deformation of filling composite geological body in loess mountainous area. *Nat. Hazards* **2022**, *110*, 1469–1493. [CrossRef]
60. Sowers, G. Compressibility of broken rock and the settlement of rockfills. In Proceedings of the 6th International Conference on Soil Mechanics and Foundation Engineering, Montreal, QC, Canada, 8–15 September 1965; pp. 561–565.
61. Charles, J. Laboratory compression tests and the deformation of rockfill structures. In *Advances in Rockfill Structures*; Springer: Dordrecht, The Netherlands, 1990; pp. 73–95.
62. Charles, J.; Skinner, H. Compressibility of foundation fills. *Proc. Inst. Civ. Eng. Geotech. Eng.* **2001**, *149*, 145–157. [CrossRef]
63. Wu, Y.; Lan, H.; Huang, W. Relationship between wave velocities and water content of unsaturated loess. *Chin. J. Geophys.* **2021**, *64*, 3766–3773.
64. Mei, Y.; Zhou, D.-B.; Hu, C.-M.; Wang, X.-Y.; Zhang, Y.; Xiao, N.; Shi, W. Study on Deformation Characteristics of Loess Ultrahigh-Fill Slope Based on Large-Scale Undisturbed Soil Centrifugal Model Tests. *Front. Earth Sci.* **2022**, *10*, 848542. [CrossRef]
65. Mesri, G.; Funk, J. Settlement of the Kansai international airport islands. *J. Geotech. Geoenviron. Eng.* **2015**, *141*, 04014102. [CrossRef]
66. Carter, M. Methods used to reduce settlements and shorten construction time at Macau international airport. *HKIE Trans.* **1996**, *3*, 1–8. [CrossRef]
67. Bennett, M.J. *Subsurface Investigation for Liquefaction Analysis and Piezometer Calibration at Treasure Island Naval Station, California*; US Geological Survey: Arcata, CA, USA, 1994; ISSN 2331-1258.